Research Article | Vol. 9, No. 6 | 1 Jun 2018 | BIOMEDICAL OPTICS EXPRESS 2743
Biomedical Optics EXPRESS

Dual-wavelength oblique back-illumination microscopy for the non-invasive imaging and quantification of blood in collection and storage bags

PATRICK LEDWIG,[1] MOSES SGHAYYER,[1] JOANNE KURTZBERG,[2,3] AND FRANCISCO E. ROBLES[1,*]

[1]*Coulter Department of Biomedical Engineering, Georgia Institute of Technology and Emory University, Atlanta, GA 30332, USA*
[2]*Carolinas Cord Blood Bank, Durham, NC*
[3]*Department of Pediatrics, Duke University Medical Center, Durham, NC 27705, USA*
[*]*robles@gatech.edu*

Abstract: There is currently no low-cost method to quantitatively assess the contents of a blood bag without breaching the bag and potentially damaging the sample. Towards this end, we adapt oblique back-illumination microscopy (OBM) to rapidly, inexpensively, and non-invasively screen blood bags for red blood cell (RBC) morphology and white blood cell (WBC) count. OBM has been recently introduced as a tomographic technique that produces high-resolution wide-field images based on phase-gradient and transmission. Here we modify this technique to include illumination at dual wavelengths to facilitate spectral analysis for cell classification. Further, we apply a modified 2D Hilbert transform to recover the phase information from the phase-gradient images for facile cell segmentation. Blood cells are classified as WBCs and RBCs, and counted based on shape, absorption spectrum, and phase profile using an automated algorithm. This work has important implications for the non-invasive assessment of (1) cell viability in storage bags for transfusion applications and (2) suitability of a cord blood collection bag for stem cell therapy applications.

OCIS codes: (180.0180) Microscopy;(350.5030) Phase; (120.5050) Phase measurement.

References and links

1. I. Moon, F. Yi, Y. H. Lee, B. Javidi, D. Boss, and P. Marquet, "Automated quantitative analysis of 3D morphology and mean corpuscular hemoglobin in human red blood cells stored in different periods," Opt. Express **21**, 30947 (2013).
2. D. B. Kim-Shapiro, J. Lee, and M. T. Gladwin, "Storage lesion: role of red blood cell breakdown," Transfus **51**, 844–851 (2011).
3. A. Hradin, R. I. Weed, and C. F. Reed, "Changes in Physical Properties of Stored Erthrocytes," Transfus **9**, 229–237 (1969).
4. B. Blasi, A. D'Alessandro, N. Ramundo, and L. Zolla, "Red blood cell storage and cell morphology," Transfus. Med. **22**, 90–96 (2012).
5. T. Bart, M. Boo, S. Balabanova, Y. Fischer, G. Nicoloso, L. Foeken, M. Oudshoorn, J. Passweg, A. Tichelli, V. Kindler, J. Kurtzberg, T. Price, D. Regan, E. J. Shpall, and R. Schwabe, "Impact of selection of cord blood units from the united states and swiss registries on the cost of banking operations," Transfus. Med. Hemotherapy (2013).
6. E. Gluckman and V. Rocha, "History of the clinical use of umbilical cord blood hematopoietic cells," Cytotherapy **7**, 219–227 (2005).
7. D. Allan, T. Petraszko, H. Elmoazzen, and S. Smith, "A review of factors influencing the banking of collected umbilical cord blood units," Stem Cells Int. **2013**, 463031 (2013).
8. C. C. Chernecky and B. J. Berger, *Laboratory Tests and Diagnostic Procedures* (Elsevier/Saunders, 2013).
9. T. N. Ford, K. K. Chu, and J. Mertz, "Phase-gradient microscopy in thick tissue with oblique back-illumination," Nat. Methods **9**, 1195–1197 (2012).
10. C. P. Saylor, "Accuracy of Microscopical Methods for Determining Refractive Index by Immersion," Part J. Res. Natl. Bureau Standards **15**, 277–294 (1935).
11. M. R. Arnison, K. G. Larkin, C. J. R. Sheppard, N. I. Smith, and C. J. Cogswell, "Linear phase imaging using differential interference contrast microscopy," J. Microsc. **214**, 7–12 (2004).

#326850 https://doi.org/10.1364/BOE.9.002743
Journal © 2018 Received 28 Mar 2018; revised 11 May 2018; accepted 12 May 2018; published 21 May 2018

Biomedical Optics EXPRESS

12. A. Tamada and M. Igarashi, "Revealing chiral cell motility by 3D Riesz transform-differential interference contrast microscopy and computational kinematic analysis," Nat. Commun. **8**, 2194 (2017).
13. G. Zheng, R. Horstmeyer, and C. Yang, "Wide-field, high-resolution Fourier ptychographic microscopy," Nat. Photonics **7**, 739–745 (2013).
14. L. Tian, X. Li, K. Ramchandran, and L. Waller, "Multiplexed coded illumination for Fourier Ptychography with an LED array microscope," Biomed. Opt. Express **5**, 2376 (2014).
15. J. Lim, H. Ding, M. Mir, R. Zhu, K. Tangella, and G. Popescu, "Born approximation model for light scattering by red blood cells," Biomed. Opt. Express **2**, 2784–2791 (2011).
16. Y. Cotte, F. Toy, P. Jourdain, N. Pavillon, D. Boss, P. Magistretti, P. Marquet, and C. Depeursinge, "Marker-free phase nanoscopy," Nat. Photonics **7**, 113–117 (2013).
17. S. Armitage, D. Fehily, A. Dickinson, C. Chapman, C. Navarrete, and M. Contreras, "Cord blood banking: volume reduction of cord blood units using a semi-automated closed system," Bone Marrow Transpl. **23**, 505–509 (1999).
18. R. Yi, K. K. Chu, and J. Mertz, "Graded-field microscopy with white light," Opt. Express **14**, 5191 (2006).
19. J. David Giese, T. N. Ford, and J. Mertz, "Fast volumetric phase-gradient imaging in thick samples," Opt. Express **22**, 1152 (2014).
20. S. B. Mehta and C. J. R. Sheppard, "Quantitative phase-gradient imaging at high resolution with asymmetric illumination-based differential phase contrast," Opt. Lett. **34**, 1924 (2009).
21. R. A. MacRae, J. A. McClure, and P. Latimer, "Spectral Transmission and Scattering Properties of Red Blood Cells*," J. Opt. Soc. Am. **51**, 1366 (1961).
22. H. P. Mansberg, A. M. Saunders, and W. Groner, "The Hemalog D White Cell Differential System," J. Histochem. Cytochem. **22**, 711–724 (1974).
23. M. R. Arnison, C. J. Cogswell, N. I. Smith, P. W. Fekete, and K. G. Larkin, "Using the Hilbert transform for 3D visualization of differential interference contrast microscope images," J. Microsc. **199**, 79–84 (2000).
24. D. English and B. R. Andersen, "Single-step separation of red blood cells, granulocytes and mononuclear leukocytes on discontinuous density gradients of Ficoll-Hypaque," J. Immunol. Methods **5**, 249–252 (1974).
25. K. G. Larkin, D. J. Bone, and M. A. Oldfield, "Natural demodulation of two-dimensional fringe patterns I General background of the spiral phase quadrature transform," J. Opt. Soc. Am. A **18**, 1862 (2001).
26. K. G. Larkin and P. A. Fletcher, "Isotropic scalar image visualization of vector differential image data using the inverse Riesz transform," Biomed. Opt. Express **5**, 907 (2014).
27. R. N. R. N. Bracewell, *The Fourier Transform and its Applications* (McGraw Hill, 2000).
28. L. Tian and L. Waller, "Quantitative differential phase contrast imaging in an LED array microscope," Opt. Express **23**, 11394 (2015).
29. C. Preza, "Rotational-diversity phase estimation from differential-interference-contrast microscopy images," J. Opt. Soc. Am. A **17**, 415 (2000).
30. G. B. Segel, G. R. Cokelet, and M. A. Lichtman, "The measurement of lymphocyte volume: importance of reference particle deformability and counting solution tonicity," Blood **57**, 894–899 (1981).
31. H. M. H. M. Shapiro, *Practical Flow Cytometry* (Wiley-Liss, 2003).
32. F. E. Robles, J. W. Wilson, and W. S. Warren, "Quantifying melanin spatial distribution using pump-probe microscopy and a 2-D morphological autocorrelation transformation for melanoma diagnosis," J. Biomed. Opt. **18**, 120502 (2013).
33. Student, "On the Error of Counting with a Haemacytometer," Biometrika. **5**, 351 (1907).
34. I. Nicoletti, G. Migliorati, M. Pagliacci, F. Grignani, and C. Riccardi, "A rapid and simple method for measuring thymocyte apoptosis by propidium iodide staining and flow cytometry," J. Immunol. Methods **139**, 271–279 (1991).
35. I. Saytashev, R. Glenn, G. A. Murashova, S. Osseiran, D. Spence, C. L. Evans, and M. Dantus, "Multiphoton excited hemoglobin fluorescence and third harmonic generation for non-invasive microscopy of stored blood," Biomed. Opt. Express **7**, 3449 (2016).
36. I. N. Rich, "Improving Quality and Potency Testing for Umbilical Cord Blood: A New Perspective," Stem Cells Transl. Med. **4**, 967–973 (2015).

1. Introduction

Blood banking is a crucial component of modern emergency medicine, as blood can be stored up to 42 days before disposal [1]. Donated blood is tested upon collection for compatibility and infectious disease, but the blood can still lose viability for transfusion over time due to a biochemical and biomechanical process known as 'storage lesion' [2]. Storage lesion occurs when blood cells in storage exhaust their glucose, leading to a loss in membrane integrity and hemolysis, and can be identified by a corresponding morphological transition of RBCs from biconcave discs to spheres [3]. Methods to assess the viability of a blood bag sample that breach the bag ultimately harm the viability of the sample [4]. Thus, there is a need for a method to cheaply and non-invasively assess the RBC morphology of a blood bag in a clinical setting to

Biomedical Optics EXPRESS

reduce the risk of post-transfusion complications and potentially extend the lifetime of a blood bag by preventing the unnecessary removal of viable samples past the set expiry date.

There is also a similar need to non-invasively quantify the total nucleated cell (TNC) count in umbilical cord blood bags for stem cell therapy applications. Umbilical cord blood has emerged as an important source of blood stem cells for use in hematopoietic stem cell therapy [5]. However, the cost of processing cord blood units (CBU) impedes its widespread acceptance, due in part to the high rate at which unsuitable samples are discarded [6]. The reasons they are discarded include low volume, processing delay, and especially low total nucleated cell count, which is strongly associated with successful hematopoietic engraftment [7]. Thus, in order to improve cost-efficacy of cord blood units as a source for stem cells, there is a need to assess the contents of the bags (i.e., TNC count) at the collection site, prior to sending the samples to a blood bank, in a way that is non-invasive (to avoid damaging the contents or compromising manufacturing), fast and low cost. Note that in this work, the WBC count is approximately equal to the TNC count given that our samples originate from a healthy male subject, from which nucleated red blood cell counts are typically low [8].

With the long-term goal of addressing these clinical limitations, we adapt oblique back-illumination microscopy (OBM), a recently developed imaging technique that provides tomographic differential phase contrast [9] to non-destructively image and quantify the contents of a blood bag at low cost and with simple operation. OBM offers high-resolution contrast based on lateral gradients in phase, allowing individual cells that are nearly transparent to be imaged without labels or dyes that would alter a blood sample [10]. Current phase contrast transmission microscopy techniques, such as differential interference contrast (DIC) [11, 12], Fourier ptychography [13, 14], quantitative phase imaging (QPI) [15], or digital holography [16], are effective at producing contrast from lateral variations in optical path-length without the need for stains or labels, but require passing light through a thin sample. The back-scattered illumination in OBM allows for the collection of transmission images from thick samples such as blood bags by configuring the system in a reflection geometry [9].

To best equip OBM to quantify blood in collection and storage bags, we implement various modifications. First, we add spectroscopic capabilities by illuminating at two wavelengths selected to more clearly distinguish WBCs from RBCs based on their absorption properties. We also produce quasi-quantitative phase images from the tomographic phase gradient information, directly available with OBM, by applying a modified 2D Hilbert transform. Lastly, we automatically classify and count WBCs using absorption, phase gradient, and phase images from each wavelength. Results show that individual cells in a dilute solution can be clearly resolved inside intact bags. This dilution need not interfere with the sterility or quantity of cells available for transfusion if blood is collected with a bag that incorporates a side compartment for this purpose [17]. We produce images that demonstrate the potential of this imaging technique for sterile RBC morphological assessment as may be used to evaluate storage lesion. Finally, for the proposed application in TNC counting in fresh umbilical cord blood, as a proof of principle, we demonstrate the ability to quantify WBC count in normal human blood samples in-bag with good agreement with typical values from literature, at a rate competitive with differential cell counting using flow cytometry.

2. Materials and methods

2.1. Oblique back-illumination microscopy

OBM was first developed by Ford *et al.* in 2012 [9]. In short, two diametrically opposed off-axis sources on the same side as the detection optics illuminate the sample, producing trans-illumination at the focus by way of multiple scattering through the thick sample (see Fig. 1). Light from alternating LED sources arrives at the detection axis obliquely. Lateral variations in index of refraction in the cells at the imaging plane create a gradient in phase delay, redirecting the

Biomedical Optics EXPRESS

obliquely-angled light toward or away from the center of the objective aperture, creating contrast in observed intensity [18]. By subtracting alternate images, a phase gradient image that rejects contributions from out-of-focus planes is produced, allowing for a tomographic cross-section of the sample at the focus depth [19]. Images with absorption-based contrast can also be produced by the sum of the two opposite oblique illumination images [20].

To enable differentiation between red and white blood cells, we have modified this technique in two ways. First, we include illumination from two sets of colors, one at 530 nm (green), and another 630 nm (red), selected to provide absorption spectral information key to performing blood cell classification. Green light transmits through the white blood cells but is absorbed by red blood cells, while red light transmits through red and white blood cells roughly equally [21,22]. Second, we render quasi-quantitative phase images, which depict the optical path length of the sample. To achieve this, consider that the contrast for the phase-gradient images arises form differential changes in optical path length with respect to the direction between the two sources (the shear direction). Thus, images of axial phase and therefore optical path length can be produced by approximating an integral of the gradient in the shear direction with a 2D analogue of the Hilbert transform [23] (see section 2.3.1).

Human blood was drawn from consenting healthy human donors by vasopuncture into heparinized tubes and diluted with phosphate-buffered saline (PBS) to 1% of pure blood concentration. All procedures adhered to approved Institutional Review Board protocols. The blood was transferred into custom-made translucent PVC bags (InstantSystems) and placed on a glass slide over the objective to flatten the bag and reduce bowing. Four LEDs (Luxeon sink-PAD II), two at 630 nm and two at 530 nm, were coupled into multimode fibers (Thorlabs FP1000ERT, numerical aperture (NA) 0.5, 1000μm diameter), each using an aspheric condenser lens (Thorlabs ACL2520U-A, NA 0.6). These wavelengths were selected to distinguish RBCs from WBCs based on their absorption spectra. These fibers directed the light into the bag, housed in a custom 3D printed objective adapter to hold each fiber ~ 6.3 mm from the center objective axis and at a 45-degree angle into the sample, each directly opposite from its own corresponding color (see inset of Fig. 1(a)). Imaging was performed on an inverted microscope (Zeiss Axiovert 200) with a 60x objective, (Nikon S Plan ELWD, NA 0.7), at a resolution of 0.6μm. The LEDs illuminated the sample individually, and light was detected with a digital camera (sCMOS pco.eddge 42LT) at 10 Hz. The illumination and camera triggering were coordinated with custom software (National Instruments LabVIEW 2017) and a data acquisition block (National Instruments SCB-68A). The objective lens was focused on cells from the blood bag suspension that had settled on the inner surface of the bag, which were illuminated by the diffuse scattering of the LED light from the fibers. Imaging from this constant plane provided a consistent cross-section of the cells in the image and reduced motion artifacts.

2.2. White blood cell isolation

In order to validate the detection of WBCs inside the blood bags, we imaged a thin layer of isolated cells. Processing for these samples proceeded as follows. First, whole blood was layered on solutions of polysucrose and sodium diatrizoate (Sigma-Aldritch Histopaque 1119 and 1077 [24]), then the buffy coat (consisting of WBCs) was separated via centrifuge. Finally, WBCs were extracted onto a glass slide and imaged with the OBM microscope. A diffuse scatterer was placed behind the specimen to simulate the effect of the diffuse light from a scattering background (Fig. 2). This was done in order to isolate and confirm the morphology and spectroscopic features of WBCs compared to RBCs as they appear in OBM images, so that the detection scheme may be validated.

Biomedical Optics EXPRESS

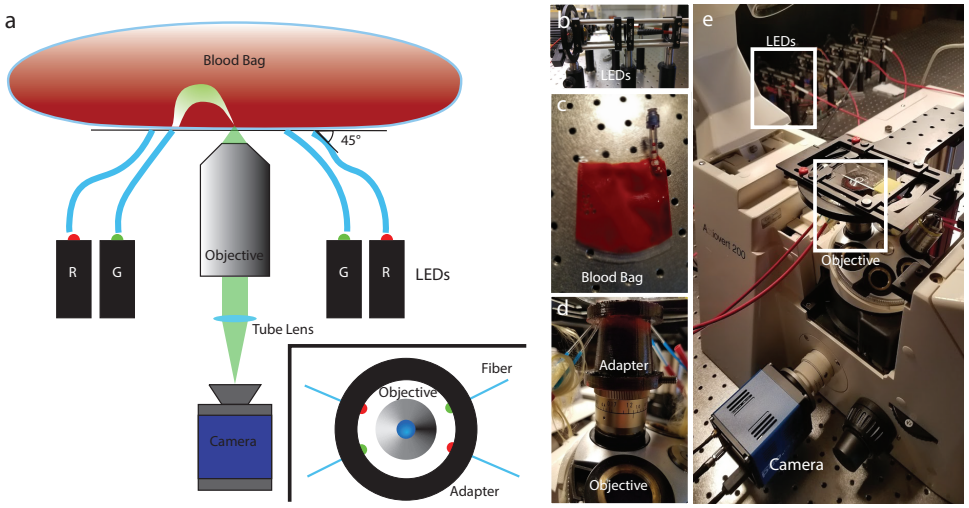

Fig. 1. (a) OBM schematic. Light epi-illuminated into the sample from two sets of two diametrically opposed LEDs enters the blood bag and is redirected into the imaging plane from the trans-direction through multiple scattering. (a Inset) Overhead diagram of objective adapter indicating LED orientation. (b) The LED fiber coupling scaffold. (c) Blood bag that is placed over the glass slide on the platform. (d) A 3D printed housing for the fibers fits snugly onto the objective below the imaging stage. (e) The inverted microscope and platform.

2.3. *Image processing*

2.3.1. Image conditioning

Image processing was performed off-line with custom software (MathWorks MATLAB 2017). Each image collected was filtered with a high-pass filter to remove low frequency contributions from features outside of the focal plane, and then normalized by the overall variance of each image. The left and right images of a given wavelength were subtracted to produce a phase gradient image, and summed to produce an image of transmission.

Next, we derive images with phase-like contrast from the phase-gradient images produced by OBM. Theoretically, images with phase contrast can be produced from the phase gradient images by integrating along the shear direction, however this process is highly susceptible to noise and ultimately produces severe streaking artifacts, making the image unrecognizable. To resolve this problem in DIC, researchers have developed a technique known as the inverse Riesz transform [11, 25]. This method reconstructs the phase by constructing a complex image by capturing phase gradients at two orthogonal shear directions, and filtering the image with a complex function in frequency space that has unit amplitude, and phase equal to the directional angle of the frequency. This filter therefore resembles a spiral ascending around the origin in phase [26]. However, because we only captured a single shear direction for each color, we used a different approach, which extends the Hilbert transform into two dimensions by filtering the image with a sign function in the direction perpendicular to the shear direction in imaginary frequency space (corresponding to spatial variations parallel to the shear direction in the image space) [23].

To illustrate how the Hilbert transform approximates an integral operation while suppressing streaking artifacts, consider a 1D integral of a finite function $f(x)$ (which models the phase gradient here) as the convolution of $f(x)$ with a step-function kernel $u(x)$ [27]

Biomedical Optics EXPRESS

$$I(x) = \int_{-\infty}^{x} f(x')dx' = \int_{-\infty}^{\infty} f(x')u(x - x')dx' \tag{1}$$

Using the convolution theorem, this can be expressed in the frequency domain as,

$$I(x) = \mathcal{F}^{-1}[F(\omega)U(\omega)] = \mathcal{F}^{-1}[(\frac{1}{i\omega} + \pi\delta(\omega))F(\omega)], \tag{2}$$

where $F(\omega)$ and $U(\omega)$ are the Fourier transforms of $f(x)$ and $u(x)$, respectively, and $\mathcal{F}^{-1}$ is the inverse Fourier transform operator. Now consider the Hilbert transform of $f(x)$ given by [27]

$$\mathcal{H}[f(x)] = \frac{1}{\pi}\int_{-\infty}^{\infty} \frac{f(x')dx'}{x' - x} = v(x) * f(x), \tag{3}$$

where $v(x) = -(\pi x)^{-1}$, and the asterisk $*$ denotes convolution. The Hilbert transform can therefore be represented as filtering $f(x)$ with the transfer function given by the Fourier transform of $v(x)$:

$$\mathcal{H}\{f(x)\} = \mathcal{F}^{-1}[F(\omega)V(\omega)] = \mathcal{F}^{-1}[(i\mathrm{sgn}(\omega))F(\omega)], \tag{4}$$

where $\mathrm{sgn}(\omega)$ is the signum function, giving -1 when $\omega < 1$, 1 when $\omega > 1$, and 0 when $\omega = 1$ [27]. The transfer functions $U(\omega)$ and $V(\omega)$ in Eq. 4 may not bear any striking resemblance in Cartesian complex space,

$$U(\omega) = \pi\delta(\omega) - \frac{i}{\omega} \tag{5}$$

$$V(\omega) = i\mathrm{sgn}(\omega). \tag{6}$$

However, examining their magnitude and phase provides useful insight. Ignoring the origin,

$$|U(\omega)| = \omega^{-1} \qquad \angle U(\omega) = -\frac{\pi}{2}\mathrm{sgn}(\omega), \qquad \omega \neq 0 \tag{7}$$

$$|V(\omega)| = 1 \qquad \angle V(\omega) = \frac{\pi}{2}\mathrm{sgn}(\omega), \qquad \omega \neq 0. \tag{8}$$

In this sense, the Hilbert transform approximates integration, but with dampened low frequencies, preserved high frequencies, and with reversed phase shift. A 2D filter can therefore be constructed as a negative imaginary signum function of the distance from the center in the direction perpendicular to the shear of the OBM image in the spatial frequency space [23].

While this method provides contrast based directly on phase displacement, more advanced image-processing techniques, such as deconvolution [28] or rotational diversity [29], that incorporate complete models of the illumination source and imaging system are required to reconstruct a fully quantitative phase map. Pending a quantitative characterization of the blood bag as a scattered illumination source, we reserve for the images we produce with this method the designation "quasi-quantitative".

Apart from producing compelling wide-field images of the cells with quasi-quantitative phase contrast, the resulting phase images were instrumental in counting and identifying individual cells with a simple procedure, as the spherical shape of WBCs stands out against the characteristic biconcave shape of erythrocytes. Moreover, this small amount of Fourier-space image processing saved a great deal of computational resources in classification.

Biomedical Optics EXPRESS

2.3.2. Cell segmentation and classification

In order to identify possible WBCs in the image, cell segmentation was performed in two steps. First, candidate WBCs were selected by a cross-correlation of the red phase gradient and green phase images with a kernel of a corresponding test image of a known WBC. Locations were selected with a threshold of the convolved image, and candidate locations were morphologically dilated with a circular element the size of a typical cell to highlight a region enclosing a candidate cell. Cell regions that were identified by both red phase gradient and green phase images were stored for comparison.

While the first step roughly identified candidates based on phase information, it was still necessary to distinguish WBCs from false positives, such as nucleated RBCs. In the second phase of processing, individual cells of any kind were identified and counted with the circular Hough transform of the binarized green phase image. The mean intensity of the red and green transmission images within the boundary of each identified circle was calculated. The intensity of the green transmission images for the WBCs was expected to be higher than that of the red transmission image, when compared to RBCs. Therefore, cell candidates selected from the first step that had a significantly higher green-to-red transmission ratio than the other cells in the image were identified as WBCs. This analysis was automated and performed for every image in a suite of 16 images collected for a given blood bag. A WBC count and total blood cell count was obtained from the tallied counts.

3. Results

3.1. Monolayer of cells in a buffy coat imaged with OBM

Isolated white blood cells were smeared across a microscope slide to confirm their appearance in the three imaging domains (phase gradient, transmission, and phase). The isolation procedure did not exclude all RBCs from the sample. However, the relative number of WBCs in the isolated solution was proportionally much higher than in whole blood, and the presence of RBCs allowed us to compare differentially the characteristics of the two respective cell types in our imaging modality.

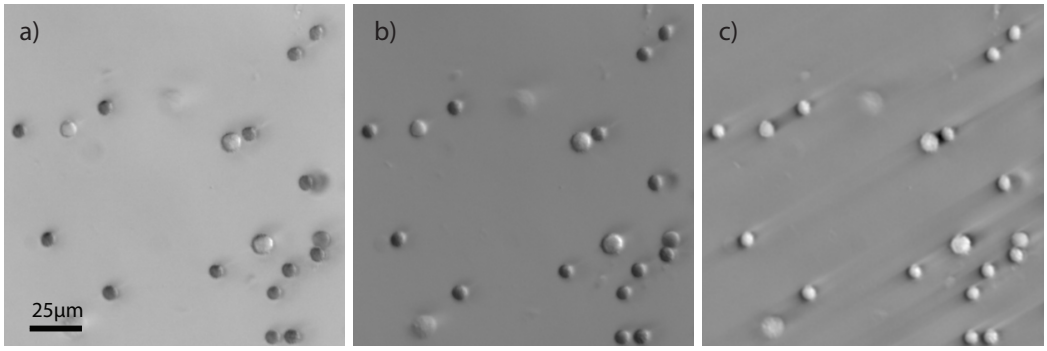

Fig. 2. An OBM image of mononuclear cell layer on a coverslip with green illumination in (a) transmission and (b) phase gradient and (c) phase.

Figure 2(a) confirms the translucence in green light and increased size as compared to the assorted RBCs that appear in the image. The RBCs in Fig. 2 appear spherical, as the process of layer separation altered the characteristic biconcave shape. Indeed, the phase image (Fig. 2(b)) confirms that both cell types are spherical, as the RBCs appear similar in shape to the WBCs, but smaller. This confirms the identity of the white blood cell in the image, and reinforces the

Biomedical Optics EXPRESS

notion that a WBC can be clearly distinguished even from RBCs that have undergone a spherical morphological transformation.

3.2. In-bag whole-blood microscopy with OBM

Sixteen images of in-bag whole blood, diluted to 1% of their original concentration with PBS were obtained, with red and green illumination, alternately (Fig. 3). As this blood was freshly drawn, very little morphological degradation can be observed in the RBCs in Fig. 3, as compared to Fig. 2. Nucleated WBCs can be clearly identified by their relatively uniform phase profile, as compared to the biconcave RBCs in the image. The green transmission image further confirms the identification of WBCs by the phase profiles with the increased intensity of transmission that was seen in the mononuclear cell isolation layer.

3.3. Identification and segmentation of nucleated cells

Morphological features from the red phase gradient (Fig. 3(b)) and green phase profile (Fig. 3(f)) images were used as a first stage in the segmentation process to determine WBC candidates. The insets of Fig. 4(a) and Fig. 4(b) show the WBC kernel used in the cross-correlation with the red phase and green phase gradient, respectively. This kernel was isolated from a test OBM whole blood image. Whole blood was used as the test image, rather than the isolation layer, so that morphological changes that the WBCs may have undergone in the isolation process (such as volume alteration in response to osmotic conditions [30]) would not affect identification.

Figure 4 shows the selected cells based on the cross-correlation of the red phase gradient image (red circles) and green phase image (green circles). Threshold values used to select WBC candidates from each individual cross-correlation were set relatively low to obtain higher sensitivity at the expense of lower specificity in this initial stage. Then, because each image highlights different features—for example, edge intensity in the phase gradient image or surface profile in the phase image—we only select cells that are identified as candidates from both types of images to pass onto the next stage.

Once the regions containing the candidate WBCs were obtained, they could be identified as white blood cells by comparing their mean transmission to the transmission of all other cells in the image. Cells identified with Hough circle detection can be seen in Fig. 5(a) (delineated by light blue lines), and a scatter plot of the transmission in green versus red can be seen in Fig. 5(b). As the reconstruction of the phase image is not strictly quantitative [23], it was necessary to identify cells with statistical analysis or machine learning. A simple two dimensional PCA is demonstrated in Fig. 5(b). Here we compare the candidate cells to the entire cell population in the image (primarily composed of RBCs) and select only the candidates that are greater than 1.5 standard deviations away from the mean in the direction of the second principal component. Note that not all cells that are above the average green-to-red transmission ratio are WBCs, so the cross-correlation step was critical in removing many potential false positives. This approach achieved 100% sensitivity and specificity in WBC detection as compared to visual inspection for our 16-image test. Further, we identified 22 WBCs and 10,058 RBCs, resulting in a WBC to RBC ratio of 2.18×10^{-3} with an error of 21.3% [31], putting our analysis within the range for a typical adult [8]. We expect that more sophisticated algorithms—for example, taking second-order morphological features into account [32]—could help sustain such results, with high sensitivity and specificity, even in larger image sets. Nevertheless, these data show that a simple and computationally efficient automated algorithm can provide robust results.

Finally, we apply a statistical analysis to gain a better understanding of the total number of WBCs that need to be sampled in order to obtain an estimate with low error (<15%) compared to total cell count in the blood bag. We model the WBC count as a Poisson counting process, a low-probability approximation of a binomially-distributed random variable, as we are only concerned with whether or not a given cell is a WBC. For humans, a typical ratio of WBCs in

Biomedical Optics EXPRESS

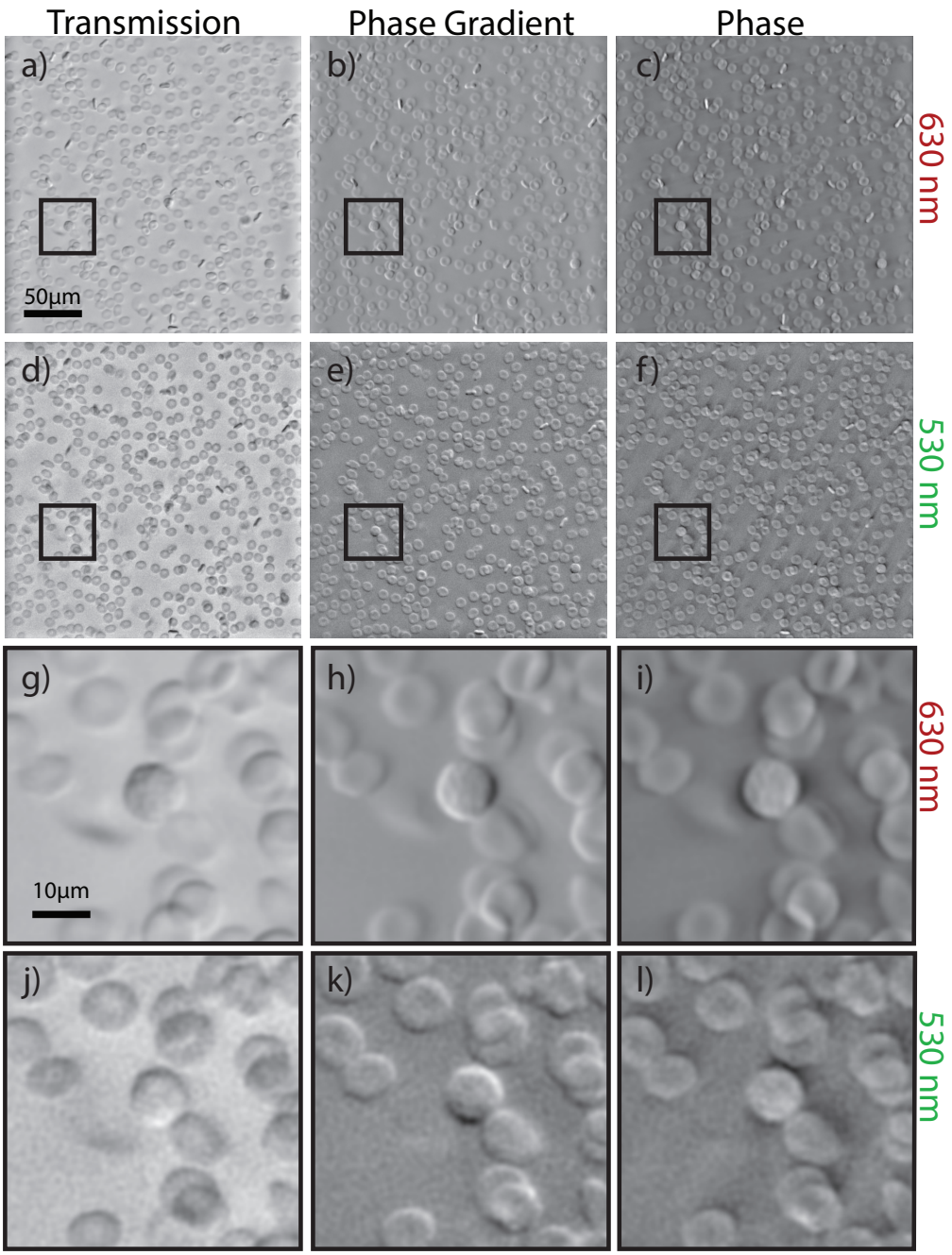

Fig. 3. OBM images of red (a) transmission, (b) phase gradient, (c) phase. (d)-(f) Corresponding green images. (g)-(l) Enlarged images of a WBC in the corresponding contrast method in (g)-(i) red and (j)-(l) green

Biomedical Optics EXPRESS

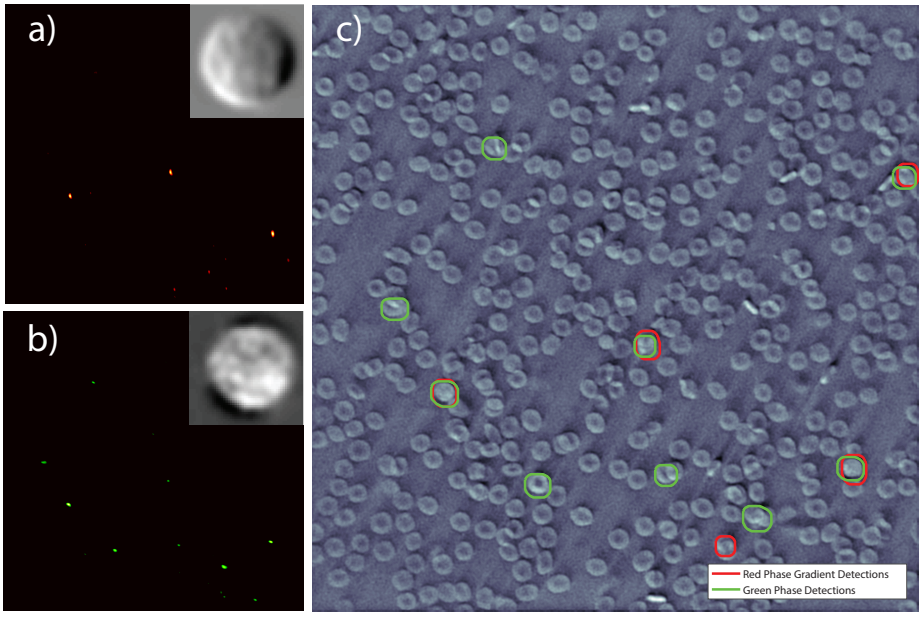

Fig. 4. Heat map of cross-correlation detection of (a) red phase gradient and (b) green phase image. Candidate cells are found in regions around values that exceed a threshold. Inset on the heat map are the corresponding WBC images used as kernels in the cross-correlation detection. (c) Region with WBC candidate overlaid onto the green phase image (see Fig. 3(f)). The cells with both the red and green circles are selected as candidates for transmission (2nd stage) analysis.

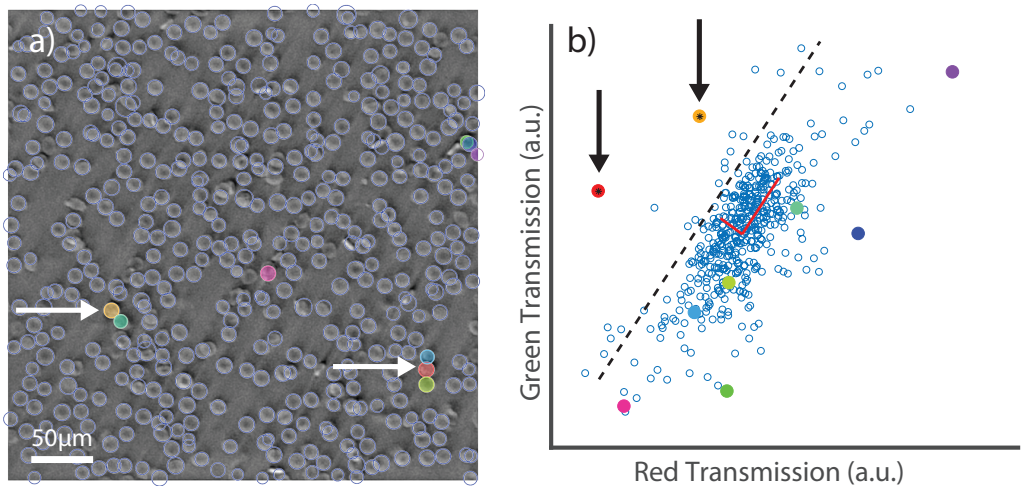

Fig. 5. The transmission stage of detection. (a) The green phase image with candidate cells highlighted in color (b) scatter of green versus red transmission of each detected cell. The points with candidate cells are given the same corresponding color as the overlay. The cells identified by eye to be WBCs (arrows, left), are correctly selected by their characteristic transmission (arrows, right). The dotted line in (b) indicates the cutoff distance beyond which candidate cells are determined to be WBCs.

Biomedical Optics EXPRESS

blood may range from 0.74×10^{-3} to 2.34×10^{-3} [8]. The standard error of a binomial distribution reduces to the coefficient of variation of a Poisson counting process for a small event rate, given by the inverse square root of the number of rare events (in this case, the number of WBCs detected) [33]. To achieve 15% standard error, therefore, we need to find at least $1/0.15^2 \approx 44$ WBCs, which, in the worst case of a standard normal blood range would require $\sim 60,000$ total cells to be imaged. To be competitive with flow cytometry, a method that destroys the counted cells, this must be a achieved on a timescale of minutes [34]. With our current configuration, we are able to capture approximately 625 cells in one field of view in 0.4 seconds. With a motorized stage and no modifications to the capture setup, a statistically significant WBC count can be obtained in under 2 minutes. However, we expect to be able to reduce this time by increasing the capture rate, obtaining a wider field of view, and increasing the concentration of blood in the bag. We estimate that a statistically significant value of the WBC population can be obtained in a matter of seconds with modest adjustments.

For this trial, we have sought to demonstrate the proof of concept, and so have only analyzed a suite of 16 images of whole blood. In this analysis, we have found 22 WBCs and 10,058 RBCs, so the number of nucleated cells per red blood cell to be $2.18\times10^{-3}\pm21.3\%$ with standard confidence, putting our analysis within the range for a typical adult [8].

4. Discussion and conclusion

Here we have demonstrated the utility of dual-wavelength OBM to provide rapid, inexpensive, and non-invasive cell classification and counting of whole blood samples in-bag. We have modified the modality to suit the clinical needs of assessing blood bag viability and counting WBCs at the exclusion of nucleated RBCs. For classification analysis, we used information gleaned from the phase gradient and transmission images, as well as spectral information obtained by illuminating at two separate wavelengths. Furthermore, we implemented an image processing technique to acquire a quasi-quantitative phase image that was invaluable in our analysis of differential cell morphology. Finally, we have developed an automated algorithm to quantify total nucleated cell count with bounds set on statistical certainty.

The high-resolution quasi-quantitative phase images which clearly depict the RBC's morphology within a blood bag may enable non-invasive detection of physical signs of storage lesion, such as fragmentation and disc-sphere transformation [3, 4]. Recent efforts to monitor blood bag content have involved breaching the bag [1], or required expensive systems that demand expertise to use [35]. On the other hand, the dual-wavelength OBM method that is presented here is ideally suited for blood bag imaging, as it achieves high-resolution tomographic images of cells within the bag without the need for expensive lasers or expert technicians. Of course, this technique would require the use of specialized bags to facilitate a sterile dilution of a portion of the blood sample.

In addition, our demonstrated ability to count nucleated white blood cells can be applied to assessing a count of TNC at the clinic. Furthermore, our collection of both morphological and spectral features has potential to be used to distinguish among certain white blood cell types to allow for a mononuclear cell (MNC) count, a much stronger predictor of successful engraftment [36].

We have demonstrated the potential of this imaging method for two clinical applications, storage lesion assessment and cord blood unit TNC counting. Future work will focus on better establishing the efficacy for each of these particular applications.

In summary, we have applied dual-wavelength OBM to non-destructively image the contents of a blood bag at low cost and with simple operation. By automating this technique to collect and analyze a suite of images, a dual-wavelength oblique back-illuminating microscope can be established as a robust, low-cost, and easy to use instrument in various clinical settings that can be operated by workers without the need for specialized training or expertise.

Biomedical Optics EXPRESS

Funding

Burroughs Welcome Fund (BWF) (1014540); The Marcus Center for Therapeutic Cell Characterization and Manufacturing (MC3M); The Georgia Tech Foundation and the Georgia Research Alliance; Wallace H. Coulter Department of Biomedical Engineering at Georgia Institute of Technology and Emory University.

Disclosures

The authors declare that there are no conflicts of interest related to this article.